J Mater Sci: Mater Electron **(2023) 34:1873**

Hybrids of porous $NiMn_2O_4$@reduced graphene oxide composites for asymmetric supercapacitor applications

P. Kanagambal[1,*], A. Jafar Ahamed[1], P. Rajeswaran[2], and T. Kamatchi[3]

[1] *PG and Research Department of Chemistry, Jamal Mohamed College (Autonomous), Affiliated to Bharathidasan University, Tiruchirappalli, Tamilnadu 620020, India*

[2] *Department of Chemistry, Vel Tech High Tech Dr.Rangarajan Dr.Sakunthala Engineering College (Autonomous), Chennai, Tamilnadu 600062, India*

[3] *Department of Chemistry, Panimalar Engineering College (Autonomous), Chennai, Tamilnadu 600123, India*

Received: 4 March 2023
Accepted: 9 September 2023
Published online: 27 September 2023

ABSTRACT

A distinctive hierarchical hybrid nanostructure which consists of ultrathin and vertical $NiMn_2O_4$ nanosheet grown on reduced graphene oxide ($NiMn_2O_4$ NSs@rGO) is synthesised by a facile hydrothermal procedure. The surface morphologies, structure, and elemental composition of the materials are examined by XRD, Raman spectroscopy, FESEM, and HRTEM and XPS. The active materials ($NiMn_2O_4$@rGO) are coated on nickel foam electrode to test the capacitance activity from cyclic voltammetry (CV), galvanostatic charge–discharge (GCD), and electrochemical impedance spectra (EIS) techniques with 1.0 M KOH. The specific capacitance of $NiMn_2O_4$@rGO is 1891 Fg^{-1} at 1 Ag^{-1}. After 5000 cycles, the specific capacitance retention rate of $NiMn_2O_4$@rGO is 80% at 20 Ag^{-1}. Besides, the assembled $NiMn_2O_4$@rGO//AC asymmetric supercapacitor (ASC) displays the maximum energy density of 49.8 $Whkg^{-1}$ at a power density of 880.5 Wkg^{-1}. Significantly, an ultralong cycling life of 98% capacitance retention is achieved for the ASC device after 5000 charge/discharge cycles at 2 Ag^{-1}. These results showed that rGO addition has increased the conductivity of $NiMn_2O_4$, and thus it can be suggested as a new technique to improve the capacitance. Moreover, the prominent cycling stability and high energy density indicate that the composites possess potential application as excellent electrode material.

1 Introduction

Since the world's fuel reserves are dwindling and pollution levels are rising to an all-time high, scientists have been compelled to explore novel methods of harnessing alternative energy. However, their intermittent nature in terms of energy production still limits their dominance over conventional coal and oil and gas energy sources, despite the fact that this energy has the potential to mitigate the major energy problem

Address correspondence to E-mail: kanagambalvarnika@gmail.com

https://doi.org/10.1007/s10854-023-11298-6

in the world. In this prospect an efficient energy storage device can be savior. Currently, scientists all over the world are putting in place various efforts to create energy storage systems such as the Na-ion battery and fuel cells. Due to their rapid charging–discharging cycle, large power density, modest energy density, and long cycle life [1, 2], supercapacitors are garnering a lot of interest. Carbon-based electrodes are used in commercial supercapacitors because of their low contact resistance and high surface area, both of which contribute to the device's high performance [3–5]. Recently, it has been discovered that mixed transition metal oxides (MTMOs), an emerging category of announcing electrode materials for a variety of energy-related uses, are produced by the sophisticated synthesis of two inexpensive transition metal oxides, resulting in the creation of single-phase MTMOs with higher electric and electrochemical characteristics than the single part. For example, $CoFe_2O_4$, $MnFe_2O_4$, $NiCo_2O_4$, $MnCo_2O_4$, $CoMn_2O_4$, and $NiMn_2O_4$ have been utilised as the active electrode materials for supercapacitor applications [6–8].

Among these, $NiMn_2O_4$ stands out for having a special spinel crystal structure and having outstanding electrochemical properties due to its many benefits such as lower cost, sustainability, and ease of preparation. There have been some advancements made using $NiMn_2O_4$ materials. $NiMn_2O_4$ with a mesoporous structure has been described by Miao Zhang and colleagues [9], $NiMn_2O_4$@CNT nanocomposite have been created by Nan's groups [10], and K. Vijaya Sankar's groups have looked into the electrochemical intercalation/de-intercalation process of it for supercapacitors [11]. Similar to other transition metal oxides, nevertheless, its uses are constrained by its low particular area of surface, poor dispersion, and generally poor conductivity [12]. We focus on integrating promising electrode materials with carbon materials in order to address the aforementioned limitations. An essential form of carbon known as graphene has a hexagonal 2D layer structure made up of sp2 carbon atoms [13]. Graphene is a promising candidate for hybrid hierarchical nanostructures composites with TMO because of its unusual structural characteristics, which include a large surface area, exceptional electricity conductivity, excellent chemical substances and thermal stability, and wide potential window [14]. The development of graphene/TMO hybrid materials has received a lot of attention recently, and as a result, such substances perform electrochemically better than their component parts individually. By virtue of its oxygen-containing groups, graphene provides a 2D foundation for the construction of conductive networks, inhibits the volume fluctuation and aggregation of TMO, and assures reliable electrical connections between graphene and TMO [15, 16]. Although there have only been a few papers on $NiMn_2O_4$/graphene composite materials for super-capacitors, it is safe to assume that these materials will have improved electrochemical performance. Thi Ngo [17] designed a 3D structure with excellent capacitance (396.85 Fg^{-1}) and very high glucose sensitivity (1310.8 μAmM^{-1} cm^{-2}), all with a quick reaction time of 3.5 s. Energy density of 60.69 $Whkg^{-1}$ and high capacitance of 151 Fg^{-1} were achieved for CNT@$NiMn_2O_4$ nanocomposites [10]. The specific capacitance of 30 wt% rGO/$NiMn_2O_4$ nanorods composites was measured at 693.00 Fg^{-1} [18]. Here, we use a simple technique to synthesise $NiMn_2O_4$@rGO composites. The mellow, simple, and inexpensive method used to prepare the product shows promising electrocatalytic activity and chemical inertness. Results from an electrochemical study showed that the composites have a specific capacitance of 693.00 Fg^{-1}, which is excellent for supercapacitors, and a notable cycling stability. Power density was 10 $kWkg^{-1}$, and energy density was 43 $Whkg^{-1}$, both of which are extremely impressive for a man-made product. Additionally, at 1 Ag^{-1}, the ASC device maintained 99% coulombic efficiency while retaining 90% of its capacitance after 10,000 cycles.

2 Materials and methods

2.1 Reactants and materials

Manganese nitrate ($Mn(NO_3)_2{\cdot}6H_2O$, purity 99.99%), nickel nitrate (Ni $(NO_3)_2{\cdot}6H_2O$, purity 99.99%), and sodium hydroxide (NaOH) were obtained from Adamas Reagent Co., Ltd. Graphene oxide slurry (LN-10R, purity 99.99%) was purchased from Levson

Co., Ltd. AC (Activated Carbon, purity 99.99%) was purchased from Fuzhou Yihuan Carbon Co., Ltd. Nickel foam was obtained from Shanxi Lizhiyuan Battery Material Co., Ltd. All chemicals were used as received without any further purification.

2.2 Synthesis of $NiMn_2O_4$ and $NiMn_2O_4$@rGO composites

Graphene oxide (GO) was synthesised from graphite powder using a reconfigured Hummers method [19]. To reduce rGO from GO, 30 ml of GO aqueous suspension (2 mg/ml) were dissolved in 120 ml of ethanol with ultrasonic stirring for 20 min. The above solution was used to dissolve and stir 1 mmol of $Ni(NO_3)_2{\cdot}6H_2O$ and 2 mmol of $Mn(NO_3)_2{\cdot}4H_2O$. The solution was mixed for 20 min under strong magnetic stirring. The solution was then dripped with 2 mL of NaOH. The remedy was collected and placed in a 100 mL reactor before being heated to 160 °C in an oven for 12 h. The eventual results reactant was freeze-dried after being washed multiple times with deionised water and ethanol. The resulting $NiMn_2O_4$/rGO powders underwent a two-hour calcination process at 500 °C (heating rate 0.5 °C min^{-1}). Pure $NiMn_2O_4$ was prepared by following the same procedure except the addition of GO. The ratio between GO and $NiMn_2O_4$ was 1:3.

2.3 Electrode preparation

$NiMn_2O_4$@rGO active material flour, conducting additive (acetylene black), and binder (polyvinylidene fluoride) were mechanically mixed together in a mass ratio of 80:10:10 to create the working electrodes. Pt wire and Ag/AgCl electrode were used as counter and reference electrodes, respectively. The powder was then placed onto a piece of nicked foil current collector after being soaked in *N*-methyl pyrrolidone to create a homogenous slurry. An area of 1 cm^2 was loaded with 1.0–2.0 mg of the prepared sample on nicked foil. Cyclic voltammetry (CV), galvanostatic charge/discharge (GCD), and electrochemical impedance spectroscopy (EIS) measurements were performed on a CH Instrument Ins to compare electrochemical outcomes with a typical three system in electrolyte solution (2 M KOH). An electrochemical workstation, model CHI 660e.

3 Results and discussion

3.1 Powder XRD analysis

X-ray powder diffraction (XRD) were used to analyse the composition and structure of the as-obtained samples on a PANalytical B.V. X'Pert PRO MPD using a CuKa radiation source (l = 1.54056 Å) worked at 40 kV and 40 mA. Figure 1, shows the XRD patterns of GO, rGO, $NiMn_2O_4$, and $NiMn_2O_4$@rGO composites. An oxygen substituent is present seen between layers of GO, as evidenced by the characteristic peaks at 2θ = 10.5°, which coincides with the (002). The disappearance of this peak in the rGO pattern is indicative of a decrease in oxygen groups as a result of the hydrothermal treatment. The diffraction peaks at 18.4°, 30.3°, 35.4°, 42.9°, 57.1°, and 63.1° were found to be associated with the (111), (220), (311), (400), (511), and (440) diffraction planes, respectively. This may be an indication of $NiMn_2O_4$ formation (JCPDS no. 01-1110) [20]. Weak peaks for the rGO and $NiMn_2O_4$ aspects can be seen in the XRD pattern of $NiMn_2O_4$@rGO, suggesting the existence of both phases in the nanocomposite.

3.2 Morphological analysis

FESEM was used to analyse the nanostructures and morphologies of $NiMn_2O_4$ NSs@rGO nanocomposites and $NiMn_2O_4$ aggregates. Figure 2a shows that $NiMn_2O_4$ ultrathin nanosheets are uniformly distributed throughout the rGO supporting surface to create

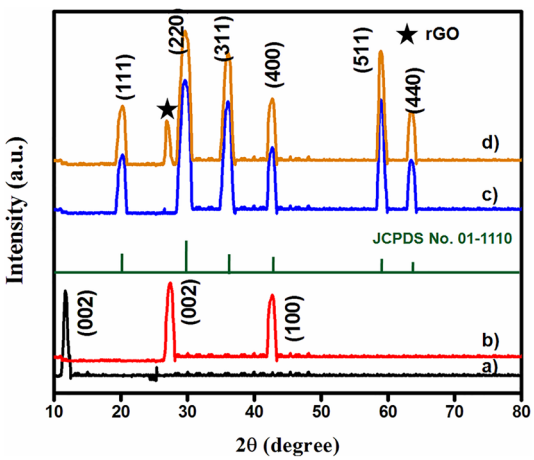

Fig. 1 XRD pattern of the electrode samples **a** GO; **b** rGO; **c** $NiMn_2O_4$; **d** $NiMn_2O_4$@rGO

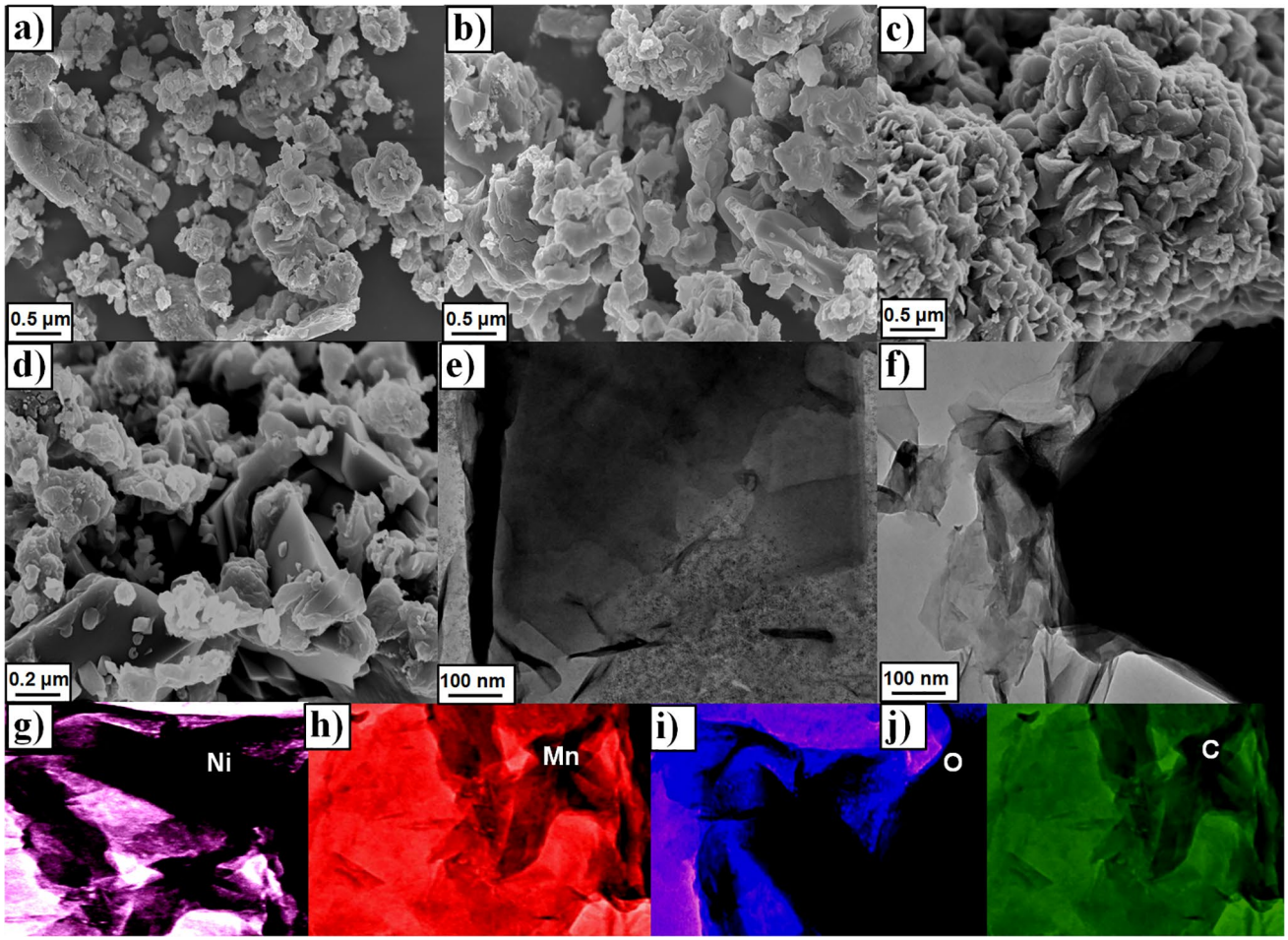

Fig. 2 **a** and **b** FESEM images of NiMn2O4@rGO with different magnifications; **c** and **d** FESEM image of $NiMn_2O_4$; **e** TEM image of $NiMn_2O_4$@rGO and **f** $NiMn_2O_4$; Elemental mapping images of **g** Ni; **h** Mn; **i** O; and **j** C

$NiMn_2O_4$ NSs@rGO. Magnification is further increased to show that the $NiMn_2O_4$ nanosheets are formed perpendicular on the rGO substrate surface, resulting in the cross-linked network structure seen in Fig. 2b. As shown in Fig. 2c, if there is no rGO supporting surface, $NiMn_2O_4$ nanosheets form spherical formations with a diameter of around 1.5 m when they come together. Figure 2d displays the microsphere's magnified picture. TEM was used to do more research on the materials' structural traits and morphological specifics. The $NiMn_2O_4$ nanosheets seen in Fig. 2e are growing randomly and vertically over rGO without any set shape, and they are around 3.2 nm in thickness. The $NiMn_2O_4$ nanosheets are made up of smaller nanoparticles and form a cross-linked network structure, as shown by Fig. 2f as well. The data shown above agree with those from the FESEM. The elemental mapping of $NiMn_2O_4$@rGO was tested and the resultant images are shown in Fig. 2g–j. The elements are Ni, Mn, O, and C and are found uniformly dispersed on the composite sample.

3.3 Raman spectra analysis

Raman spectra of rGO, $NiMn_2O_4$, and $NiMn_2O_4$@rGO composites are shown in Fig. 3. Two distinct peaks, at 1339 cm^{-1} and 1584 cm^{-1}, were found in rGO Raman spectra, which correlate to the D and G bands of rGO, respectively [21, 22]. Assigning the broad peaks at 681 cm^{-1} wavenumber to stretching vibrations of $NiMn_2O_4$ cubic spinel phases has been demonstrated [23]. The Raman spectrum of the sample $NiMn_2O_4$@rGO clearly shows that the distinctive bands of rGO and $NiMn_2O_4$ coexist, showing that they are well mixed, which is consistent with the above-mentioned XRD data. Additionally, the intensity ratio of D to G

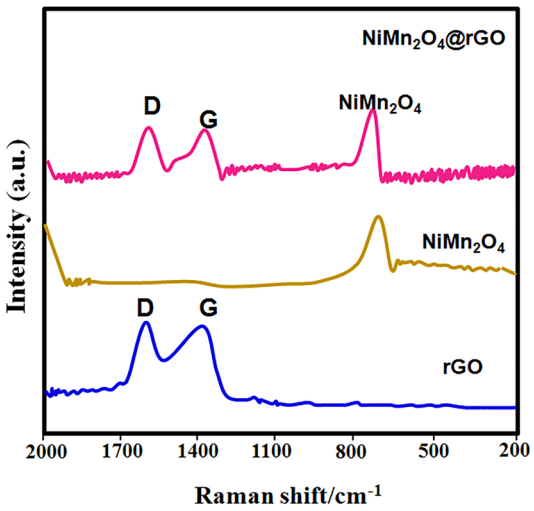

Fig. 3 Raman spectra of the electrode samples

(ID/IG) for rGO and $NiMn_2O_4$@rGO was around 1.08 and 1.13, respectively, indicating the presence of an interaction between rGO and $NiMn_2O_4$.

3.4 BET and XPS analysis

N_2 sorption experiments were used to examine the $NiMn_2O_4$ and $NiMn_2O_4$@rGO materials' tribological qualities (Fig. 4a). Type IV isotherms, typical of compounds [24–28], can be applied to all of the aforementioned substances. It was determined that $NiMn_2O_4$ had an estimated SBET of 39.2 m^2/g, while $NiMn_2O_4$@rGO composites had an SBET of 101.7 m^2/g. The pore diameter distribution curves (Fig. 4a inset) show that mesopores, with sizes ranging from 2 to 50 nm, are present in all of the samples and result from the uneven layering of rGO. GO and rGO's respective C 1s XPS spectra are shown in Fig. 4b. During the hydrothermal treatment, GO was depleted as shown by a reduction in the strength of the C–O/C=O peaks in the rGO sample compared to that of GO. Figure 4c shows the survey spectra for NiMn2O4 and $NiMn_2O_4$@rGO materials. Ni^{2+} $2p_{1/2}$ and $2p_{3/2}$ (centred at 874.1 and 856.3 eV, respectively) [29] and Mn^{3+} $2p_{1/2}$ and $2p_{3/2}$ (centred at 653.2 and 641.7 eV, to between) [30] are credited to the peaks in the $NiMn_2O_4$ sample (Fig. 4d

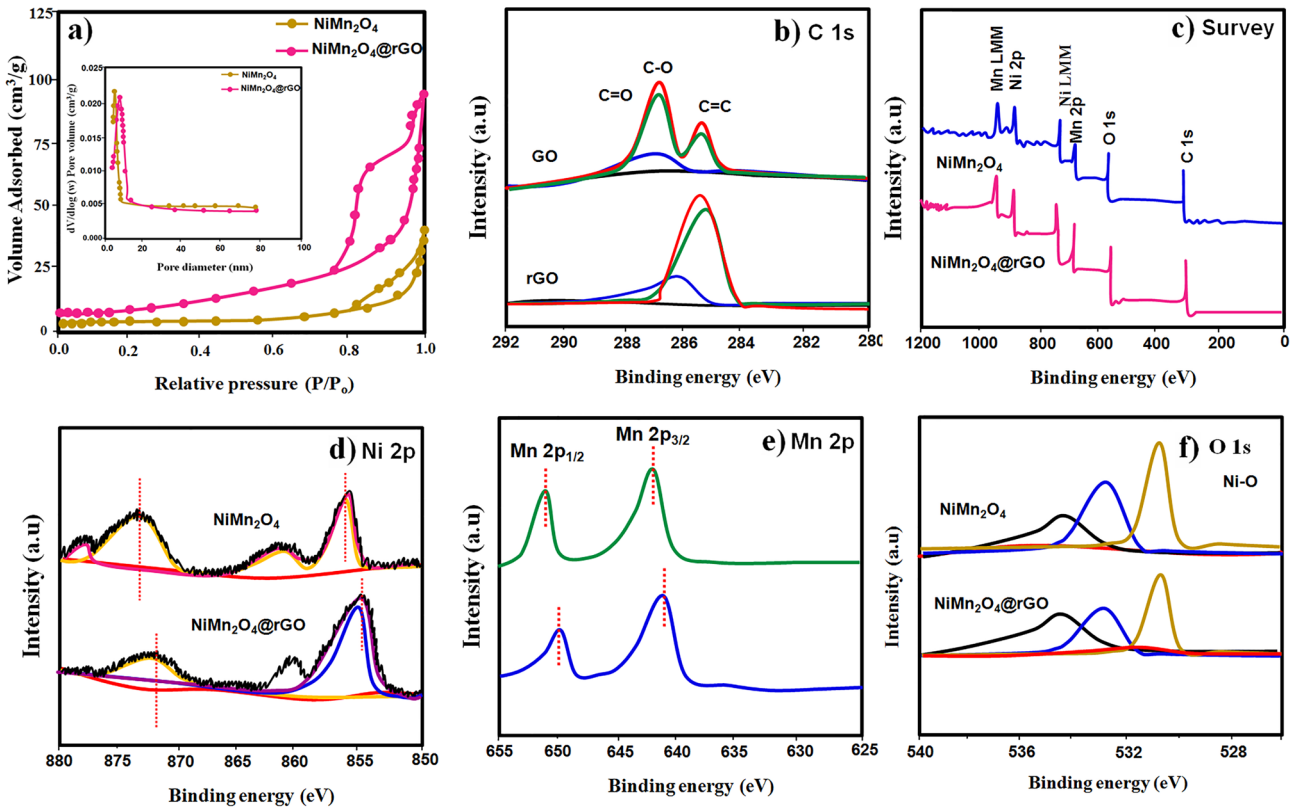

Fig. 4 **a** BET surface and pore size curves (inset) of $NiMn_2O_4$ and $NiMn_2O_4$@rGO composite samples; **b** C 1s; **c** survey; **d** Ni 2p; **e** Mn 2p; and **f** O 1s spectra of $NiMn_2O_4$ and $NiMn_2O_4$@rGO samples

and e, respectively). Sample $NiMn_2O_4$'s Ni 2p and Mn 2p peaks, on the other hand, shifted towards that lower binding energy when compared to $NiMn_2O_4$; this difference suggests that graphene materials can boost the conduction electrons density of surface Ni and Mn atoms. $NiMn_2O_4$'s O 1s high-resolution XPS spectrum (shown in Fig. 4f) [31] exhibits three fitted peaks, which conform to adsorbed H_2O (OA, at 533.2 eV), hydroxyl oxygen (OH, at 532.0 eV), and lattice oxygen (OL, at 530.5 eV).

3.5 Electrochemical performance three-electrode system

CV tests are made on a three-electrode setup with a 2 M KOH aqueous electrolyte to assess the electrode materials' electrochemical behaviour. The redox peaks in the CV curves of $NiMn_2O_4$ and $NiMn_2O_4$@rGO can be seen in Fig. 5a, b, which display the materials at a range of scan rates (10–100 mVs^{-1}) and potential windows (0.0–0.6 V). These maximums show that the Faradic reaction plays a significant role in regulating the capacitive behaviour [32]. $NiMn_2O_4$@rGO NFs electrode shows an increased incorporated area underneath the CV curve due to the addition of rGO. This is a result of the synergistic response of Ni–Mn oxides and rGO, and it indicates an increase in capacity. $NiMn_2O_4$@rGO electrode has a higher specific capacity than bare $NiMn_2O_4$ (901 Fg^{-1} at 10 mVs^{-1}) at 1221 Fg^{-1} (Fig. 5c). Linear reliance of peak cathodic and anodic current densities on scan rates is shown in Fig. 5d. Also, it proves that the synthesised electrode materials are hybrid supercapacitors. The surface coverage (Γ*) of redox species over the electrode samples are calculated based on the previous reported work [33]: we determine the concentrations of various species over electrode samples. The $NiMn_2O_4$@rGO electrode has a higher calculated value of linear reliance of peak cathodic and anodic current densities on scan rates is shown in 5d. Also, it proves that the synthesised electrode materials are hybrid supercapacitors. The surface coverage (Γ*) of redox species over the electrode samples are calculated based on the previous reported work [33]: we determine the concentrations of various species over electrode samples. The $NiMn_2O_4$@rGO electrode has a higher calculated value of (Γ*) (8.1105 $molcm^{-2}$) than the bare $NiMn_2O_4$ electrode. $NiMn_2O_4$@rGO electrode may have a greater value of (Γ*) because of the interconnected and combined surface of numerous hairy

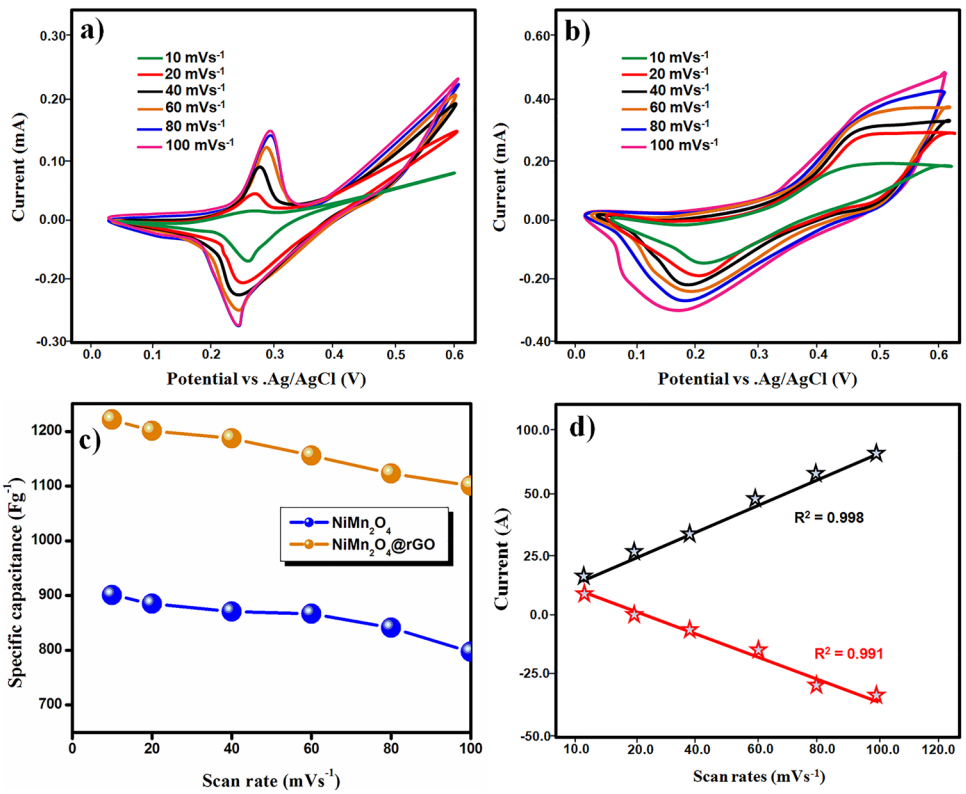

Fig. 5 Electrochemical performance of $NiMn_2O_4$ and $NiMn_2O_4$@rGO composite electrodes CV curves of **a** $NiMn_2O_4$; **b** $NiMn_2O_4$@rGO with various scan rates; **c** specific capacitance values as a function of various scan rates; **d** cathodic and anodic peak current density of $NiMn_2O_4$ and $NiMn_2O_4$@rGO composite electrodes

needle-like porous structures of $NiMn_2O_4$ and large surface area of rGO sheets. GCD measurements are used to learn more about the electrochemical behaviour of the synthesised materials. As can be seen in Fig., GCD measurements performed in the range of 0.0 to +0.06 V vs. Ag/ AgCl yielded the expected results. At a current density of 2 A/g, as shown in Fig. 6a, the charge/discharge time for the $NiMn_2O_4$@rGO electrode is significantly longer than that of pure $NiMn_2O_4$. GCD curves of $NiMn_2O_4$@rGO electrodes at varying current densities are displayed in Fig. 6b. All GCD curves are found to be nearly symmetrical, which indicates a high coulombic efficiency of the electrode materials across a wide range of current densities. $NiMn_2O_4$@rGO electrode Cs = 1848 Fg^{-1}, 1801 Fg^{-1}, 1767 Fg^{-1}, 1701 Fg^{-1}, and 1687 Fg^{-1} at 1, 2, 6, 10, and 20 Ag^{-1} current densities, respectively (Fig. 6c). Even at 20 Ag^{-1} current density, the electrode maintained up to 80% of its Cs (353 Fg^{-1}). It is an indication of increased capacitive retention of electrode materials. Cycle life estimates for the $NiMn_2O_4$ and $NiMn_2O_4$@rGO composite electrode are shown in Fig. 6d, e, which depicts the results of a continuous charge–discharge test at 1 Ag^{-1}. After one thousand charge–discharge cycles, the hierarchical nanosheet array $NiMn_2O_4$@rGO composite still maintained about 90% of its maximum capacitance, proving its long-term electrochemical stability even at high current densities. The improved electrochemical performance of the composite samples is due to the following reasons: (1) The contact of the rGO nanosheets and the $NiMn_2O_4$ nanosheets provides the good structural stability and mechanical resilience, and prevents the pulverisation of $NiMn_2O_4$, which is the cause of the better electrochemical performance of the $NiMn_2O_4$@rGO. (2) The rGO surface's capacitance for the Faradaic redox response and the rates of ion diffusion and transport of electrons are significantly increased by the composition of the composite $NiMn_2O_4$@rGO. (3) The synergetic effect between $NiMn_2O_4$ and rGO, which siginificantly improve the electrochemical performance due to the high electrical conductivity by the formation of ultra thin sheet like morphology. In order to better understand the interfacial properties of $NiMn_2O_4$@rGO, an EIS analysis was conducted on the mixture. As shown in Fig. 6(f), the Nyquist plots of the $NiMn_2O_4$@rGO composite electrode are a semicircle at high frequency region due to the Rct at the electrode interface, and a low-frequency inclined line

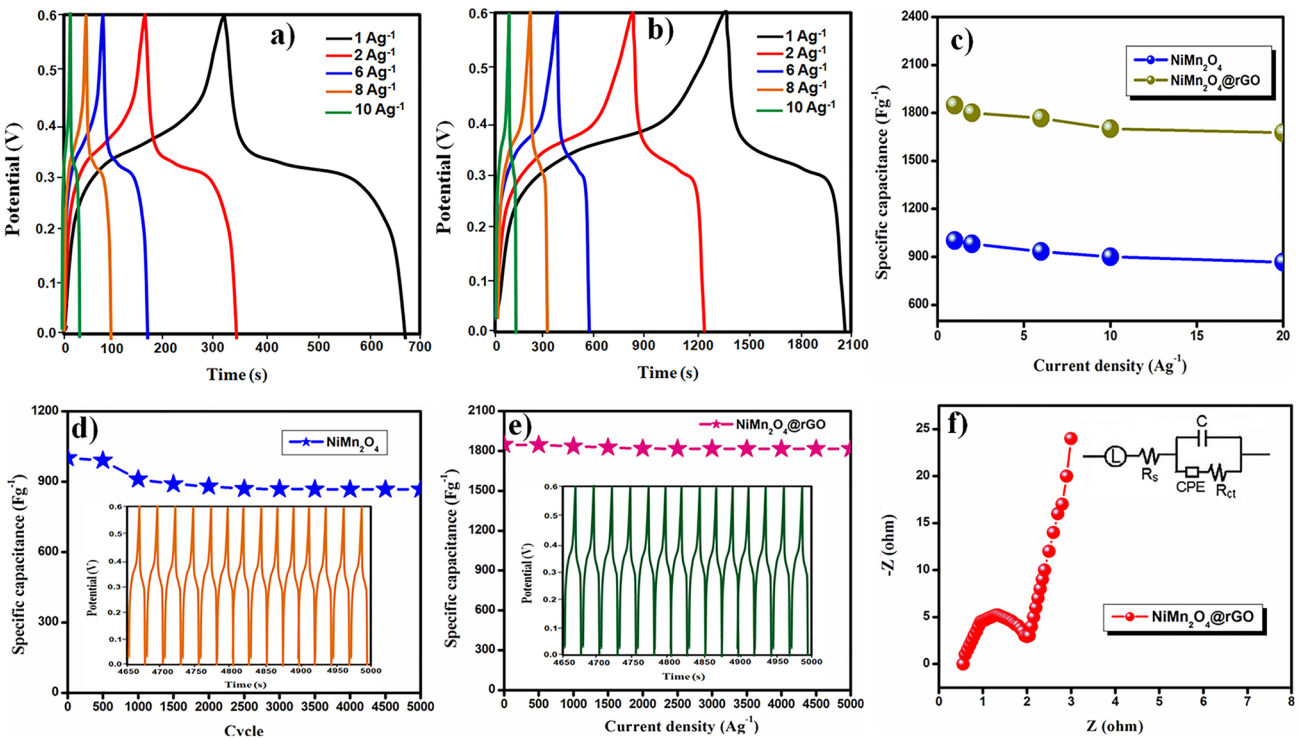

Fig. 6 GCD profile of **a** $NiMn_2O_4$; **b** $NiMn_2O_4$@rGO with various current densities; **c** specific capacitance values as a function of various current density; retention curves of **d** $NiMn_2O_4$; **e** $NiMn_2O_4$@rGO; **f** EIS curve of $NiMn_2O_4$ and $NiMn_2O_4$@rGO composite samples

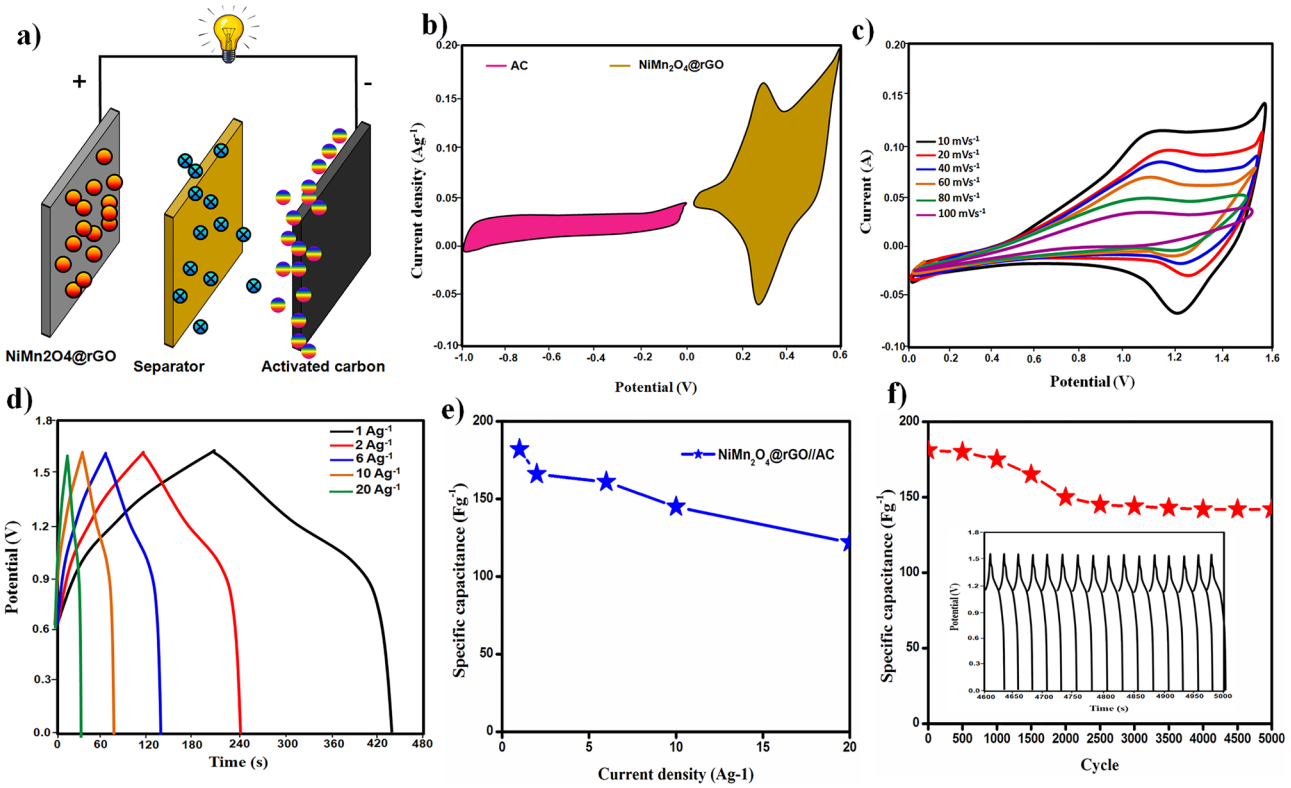

Fig. 7 **a** schematic representation of the fabricated $NiMnO_4$@rGO//AC ASC device; **b** CV curves of $NiMn_2O_4$ and AC; **c** CV curves of ASC with different sweep rates; **d** GCD curve of ASC with different current densities; **e** capacitance values as a function current density; **f** cycling performance of ASC (inset last 500 cycles)

(W: Warburg impedance) that ascribes to the diffusion of ions in the electrolyte to the electrode interface. The EIS spectra can be fitted to obtain an estimate of the semicircle's diameter, Rct. The $NiMn_2O_4$@rGO electrode's low Rct value of 6.5 Ω demonstrates the improved electrical conductivity and low electrochemical resistance.

3.6 Electrochemical performance of $NiMn_2O_4$@rGO//AC in a two-electrode system

An asymmetrical supercapacitor (ASC) was constructed in 2 M KOH aqueous electrolyte with $NiMn_2O_4$/rGO and activated carbon (AC) as the positive and negative electrodes, including both, to investigate the practical viability of the $NiMn_2O_4$/rGO composite electrode. Figure 7a is a schematic of the final ASC device before it is used. The scan rate of 10 mVs^{-1} in Fig. 7b displays the CV curves of

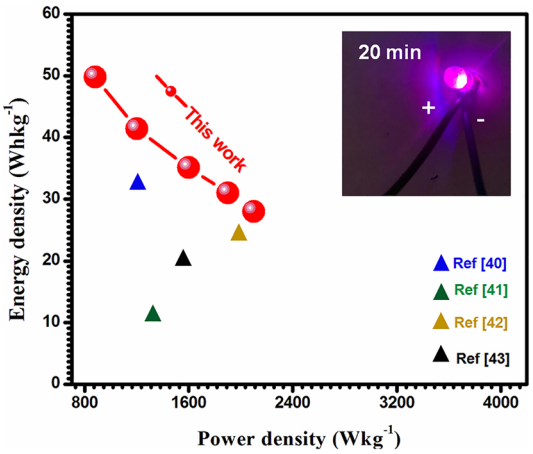

Fig. 8 A Ragone plot (energy density vs. power density) for the $NiMn_2O_4$@RGO//AC asymmetric supercapacitor device with various supercapacitor data from the literature and fabricated LED device (inset)

Table 1 Comparison of electrochemical performance between $NiMn_2O_4$@rGO and other Ni–Mn oxide/carbonaceous-based electrode materials

Electrode material	Electrolyte	3-Electrode specific capacitance	Refs.
$NiMn_2O_4$ microsphere	1 M Na_2SO_4	768.9 Fg^{-1} @ 1 Ag^{-1}	[34]
$NiMn_2O_4$/rGO/PANI	3 M KOH	757 Fg^{-1} @ 1 Ag^{-1}	[35]
$NiMn_2O_4$ on 3D N_2-doped graphene	3 M KOH	1308.2 Fg^{-1} @ 1 Ag^{-1}	[36]
$NiMn_2O_4$ @ CoS Core–Shell microspheres	2 M KOH	1751 Fg^{-1} @ 1 Ag^{-1}	[37]
MWCNT blended $NiMnO_3$/$NiMn_2O_4$	2 M KOH	1347 Fg^{-1} @ 5 Ag^{-1}	[38]
$NiMn_2O_4$@rGO	2 M KOH	1848 Fg^{-1}@1 Ag^{-1}	This work

both the $NiMn_2O_4$/rGO and the AC electrode. Given that the positive electrode has a potential window of 0 to 0.6 V and the negative electrode has a potential window of − 1.0 to 0 V, the estimated operating voltage of the $NiMn_2O_4$/rGO/AC ASC is 1.8 V. The ASC's CV curves are shown in Fig. 7c in a variety of scan rates (10–100 mVs^{-1}). The electrochemical features of double-layer capacitance and pseudocapacitance are represented by a quasi-rectangular frame with prominent redox peaks. CV curves almost maintain their original shape without polarisation as the scan rate rises, indicating the device's high rate functionality. The GCD profile of an ASC device is depicted in Fig. 7d. Using the GCD curves as depicted in Fig. At 1, 2, 6, 10, and 20 Ag^{-1}, the calculated specific capacitance of the ASC is 182.3, 166.8, 161.3, 145.1, and 121.6 Fg^{-1}, respectively (see Fig. 7e). A good rate achievement is indicated by a capacitance retention of around 72% as the current density is increased 20-fold from 1 to 20 A g^{-1} (Fig. 7f). Recent findings for the supercapacitor electrode $NiMn_2O_4$@rGO are shown in Table 1 [34–38]. The nanocomposite's enhanced conductivity and electron transfer path can be credited to the potent combination of rGO and $NiMn_2O_4$, as demonstrated by the composite's remarkably high capacitance and capacitance retention. It also shows that the electrochemical double-layer capacitance and the Faradaic redox reaction are facilitated by the $NiMn_2O_4$'s structure being modified through rGO. The efficiency of an ASC device can be measured in part by its energy density and power density. Ragone plot (Fig. 8) reveals that the $NiMn_2O_4$@rGO/AC ASC device provides a high energy density of 49.8 $Whkg^{-1}$ at a power density of 880.5 Wkg^{-1}. At a power density of 2100 Wkg^{-1}, the energy density of 28.2 $Whkg^{-1}$ is still maintained. As an added bonus, the energy density of the results obtained in this work is significantly higher than that of other $NiMn_2O_4$-based ASC devices [23, 39–41]. Additional proof of its potential, two ASC devices linked in series can power a blue LED strip for 8 min or light a violet LED for roughly 20 min (inset Fig. 8).

4 Conclusions

A simple one-step hydrothermal method was used to satisfactorily concoct hierarchical $NiMn_2O_4$@rGO electrodes. The $NiMn_2O_4$/rGO composite electrode achieves a high specific capacitance of 1848 Fg^{-1} and good rate abilities with 80% capacitance retention thanks to the novel effect of using electroactive $NiMn_2O_4$ as spacers to separate rGO nanosheets and the tight adhesion of the active materials on the current collector. Synergistic effects between the enhanced electric conductivity of rGO nanosheets and the redox characteristic of binary metal oxide are responsible for the good electrochemical conscious actions for $NiMn_2O_4$@rGO electrode. These effects include an increase in the rate of ion diffusions and electron transfers, an enhancement of the electrochemical double-layer capacitance for the surface of rGO, and a boost in the Faradaic redox reaction of near the surface of $NiMn_2O_4$. Based on these findings, $NiMn_2O_4$@rGO material may be a promising option for high-performance materials for electrodes in energy storage systems.

Author contributions

PK and AJA: study conceptualisation and writing (original draft) the manuscript. PR and TK: data curation, formal analysis, and writing (review and editing).

Funding

The authors have not disclosed any funding.

Data availability

The data that support the findings of this study are available from the corresponding author, upon reasonable request.

Declarations

Conflict of interest The authors declare that there are no conflict of interest regarding the research work reported in this manuscript.

References

1. A. González, E. Goikolea, J.A. Barrena, R. Mysyk, Review on supercapacitors: technologies and materials. Renew. Sustain. Energy Rev. **58**, 1189–1206 (2016)
2. G. Wang, L. Zhang, J. Zhang, A review of electrode materials for electrochemical supercapacitors. Chem. Soc. Rev. **41**, 797–828 (2012)
3. T. Chen, L. Dai, Carbon nanomaterials for high-performance supercapacitors. Mater. Today. **16**, 272–280 (2013)
4. A. Borenstein, O. Hanna, R. Attias, S. Luski, T. Brousse, D. Aurbach, Carbon-based composite materials for supercapacitor electrodes: a review. J. Mater. Chem. A **5**, 12653–12672 (2017)
5. L.L. Zhang, X.S. Zhao, Carbon-based materials as supercapacitor electrodes. Chem. Soc. Rev. **38**, 2520–2531 (2009)
6. F. Gongduan, L. Yao, Y. Wang, X. Peng, J. Xu, S. Pang, K. Xu, B. Du, J. Chen, Z. Hong, The dual pathway mechanisms of peroxyacetic acid activation by $CoMn_2O_4$ spinel for efficient levofloxacin degradation. J. Environ. Chem. Eng. **11**, 109774 (2023)
7. M. Subramanian, M. Shanmugavadivel, Fabrication of $NiMn_2O_4$ nanospheres and its hybrid with polyaniline for high energy and high power supercapacitor with long cycle stability. Mater. Sci. Engineering: B **294**, 116553 (2023)
8. Y. Cuixia Cheng, G. Cheng, Lai, $CuMn_2O_4$ hierarchical microspheres as remarkable electrode of supercapacitors. Mater. Lett. **317**, 132102 (2022)
9. M. Zhang, S. Guo, L. Zheng, G. Zhang, Z. Hao, L. Kang, Z.-H. Liu, Preparation of $NiMn_2O_4$ with large specific surface area from an epoxide-driven sol-gel process and its capacitance. Electrochim. Acta. **87**, 546–553 (2013)
10. H. Nan, W. Ma, Z. Gu, B. Geng, X. Zhang, Hierarchical $NiMn_2O_4$@CNT nanocomposites for high-performance asymmetric supercapacitors. RSC Adv. **5**, 24607–24614 (2015)
11. K. Vijaya Sankar, S. Surendran, K. Pandi, A.M. Allin, V.D. Nithya, Y.S. Lee, K. Selvan, Studies on the electrochemical intercalation/de-intercalation mechanism of $NiMn_2O_4$ for high stable pseudocapacitor electrodes. RSC Adv. **5**, 27649–27656 (2015)
12. W. Chen, R.B. Rakhi, Q. Wang, M.N. Hedhili, H.N. Alshareef, Morphological and electrochemical cycling effects in MnO_2 nanostructures by 3D electron tomography. Adv. Funct. Mater. **24**, 3130–3143 (2014)
13. A. Majeed, W. Ullah, A.W. Anwar, F. Nasreen, A. Sharif, G. Mustafa, A. Khan, Graphene-metal oxides/hydroxide nanocomposite materials: fabrication advancements and supercapacitive performance. J. Alloys Compd. **671**, 1–10 (2016)
14. E.R. Ezeigwe, M.T.T. Tan, P.S. Khiew, C.W. Siong, Solvothermal synthesis of graphene–MnO_2 nanocomposites and their electrochemical behavior. Ceram. Int. **41**, 11418–11427 (2015)
15. Z.-S. Wu, G. Zhou, L.-C. Yin, W. Ren, F. Li, H.-M. Cheng, Graphene/metal oxide composite electrode materials for energy storage. Nano Energy. **1**, 107–131 (2012)
16. P.S. Shewale, K.-S. Yun, Ternary nanocomposites of PEDOT: PSS, RGO, and urchin-like hollow microspheres of $NiCo_2O_4$ for flexible and weavable supercapacitors. Mater. Sci. Eng: B **292**, 116404 (2023)
17. Y.L.T. Ngo, L. Sui, W. Ahn, J.S. Chung, S.H. Hur, $NiMn_2O_4$ spinel binary nanostructure decorated on three-dimensional reduced graphene oxide hydrogel for bifunctional materials in non-enzymatic glucose sensor. Nanoscale. **9**, 19318–19327 (2017)
18. Z. Wang, Z. Zhu, C. Zhang, C. Xu, C. Chen, Facile synthesis of reduced graphene oxide/$NiMn_2O_4$ nanorods hybrid materials for high-performance supercapacitors. Electrochim. Acta. **230**, 438–444 (2017)
19. W.S. Jr Hummers, R.E. Offeman, Preparation of graphitic oxide. J. Am. Chem. Soc. **80**, 1339–1339 (1958)
20. S.Y. Sawant, V.M.S. Verenkar, S.C. Mojumdar, Preparation, thermal XRD, chemical and FTIR spectral analysis of $NiMn_2O_4$ nanoparticles and respective precursor. J. Therm. Anal. Calorim. **90**, 669–672 (2007)
21. J. Ye, L. Ma, W. Chen, Y. Ma, F. Huang, C. Gao, J.Y. Lee, Supramolecule-mediated synthesis of MoS_2/reduced graphene oxide composites with enhanced electrochemical

performance for reversible lithium storage. J. Mater. Chem. A **3**, 6884–6893 (2015)
22. Z. Yang, H. Zhang, B. Ma, L. Xie, Y. Chen, Z. Yuan, K. Zhang, J. Wei, Facile synthesis of reduced graphene oxide/tungsten disulfide/tungsten oxide nanohybrids for high performance supercapacitor with excellent rate capability. Appl. Surf. Sci. **463**, 150–158 (2019)
23. Y.T. Ngo, L. Sui, W. Ahn, J.S. Chung, S.H. Hur, $NiMn_2O_4$ spinel binary nanostructure decorated on three dimensional reduced graphene oxide hydrogel for bifunctional materials in non-enzymatic glucose sensor. Nanoscale. **9**, 19318–19327 (2017)
24. R. BoopathiRaja, M. Parthibavarman, Hetero-structure arrays of $MnCo_2O_4$ nanoflakes@nanowires grown on ni foam: design, fabrication and applications in electrochemical energy storage. J. Alloy Compd. **811**, 152084 (2019)
25. R. BoopathiRaja, M. Parthibavarman, A. Nishara, Begum, Hydrothermal induced novel $CuCo_2O_4$ electrode for high performance supercapacitor applications. Vacuum. **165**, 96–104 (2019)
26. R. BoopathiRaja, M. Parthibavarman, Desert rose like heterostructure of $NiCo_2O_4$/NF@PPy composite has high stability and excellent electrochemical performance for asymmetric super capacitor application. Electrochim. Acta **346**, 136270 (2020)
27. R. BoopathiRaja, M. Parthibavarman, Reagent induced formation of $NiCo_2O_4$ with different morphologies with large surface area for high performance asymmetric supercapacitors. Chem. Phys. Lett. **755**, 137809 (2020)
28. M. Jayashree, M. Parthibavarman, S. Prabhakaran, Hydrothermal-induced α-Fe_2O_3/graphene nanocomposite with ultrahigh capacitance for stabilized and enhanced supercapacitor electrodes. Ionics. **25**, 3309–3319 (2019)
29. P. Sun, C. Wang, W. He, P. Hou, X. Xu, One-step synthesis of 3D network-like $NixCo_{1-x}MoO_4$ porous nanosheets for high performance battery-type hybrid supercapacitors. ACS Sustain. Chem. Eng **5**, 10139–10147 (2017)
30. J. Liu, X. Ge, X. Ye, G. Wang, H. Zhang, H. Zhou, Y. Zhang, H. Zhao, 3D graphene/δ-MnO_2 aerogels for highly efficient and reversible removal of heavy metal ions. J. Mater. Chem. A **4**, 1970–1979 (2016)
31. L. Lu, H. Tian, J.H. He, Q.W. Yang, Graphene-MnO_2 hybrid nanostructure as a new catalyst for formaldehyde oxidation. J. Phys. Chem. C **120**, 23660–23668 (2016)
32. C. Zhang, C. Lei, C. Cen, S. Tang, M. Deng, Y. Li, Y. Du, Interface polarization matters: enhancing supercapacitor performance of spinel $NiCo_2O_4$ nanowires by reduced graphene oxide coating. Electrochim. Acta. **260**, 814–822 (2018)
33. A.K. Das, R.K. Layek, N.H. Kim, D. Jung, J.H. Lee, Reduced graphene oxide (RGO)-supported $NiCo_2O_4$ nanoparticles: an electrocatalyst for methanol oxidation. Nanoscale. **6**, 10657–10665 (2014)
34. Y. Sun, J. Zhang, X. Sun, N. Huang, High-performance spinel $NiMn_2O_4$ microspheres self-assembled with nanosheets by microwave assisted synthesis for supercapacitors. CrystEngComm. **22**, 1645–1652 (2020)
35. W. Kang, Y. Tang, W. Li, X. Yang, H. Xue, Q. Yang, C. Lee, High interfacial storage capability of porous $NiMn_2O_4$/C hierarchical tremella-like nanostructures as the lithium ion battery anode. Nanoscale. **7**, 225–231 (2015)
36. M.R. Kim, M. Naidukalla, S. Kim, M. Kim, I. Kim, $NiMn_2O_4$ nanosheet-decorated hierarchically porous polyaromatic carbon spheres for high-performance supercapacitors. Chem. Electro Chem. **4**, 1214–1221 (2017)
37. H. Wei, J. Wang, L. Yu, Y. Zhang, D. Hou, T. Li, Facile synthesis of $NiMn_2O_4$ nanosheet arrays grown on nickel foam as novel electrode materials for high-performance supercapacitors. Ceram. Int. **42**, 14963–14969 (2016)
38. S. Karmakar, D. Behera, Small polaron hopping conduction in $NiMnO_3$/$NiMn_2O_4$ nano-cotton and its emerging energy application with MWCNT. Ceram. Int. **45**, 13052–13066 (2019)
39. S. Sahoo, S. Zhang, J. Shim, Porous ternary high performance supercapacitor electrode based on reduced graphene oxide, NiMn2O4, and polyaniline. Electrochim. Acta. **216**, 386–396 (2016)
40. C.-Y. Lee, S.-J. Kim, I.-S. Hwang, J.-H. Lee, Glucose-mediated hydrothermal synthesis and gas sensing characteristics of WO_3 hollow microspheres. Sens. Actuators B **142**, 236–242 (2009)
41. K.V. Sankar, S. Surendran, K. Pandi, A.M. Allin, V.D. Nithya, Y.S. Lee, Studies on the electrochemical intercalation/de-intercalation mechanism of $NiMn_2O_4$ for high stable pseudocapacitor electrodes. RSC Adv. **5**, 27649–27656 (2015)